Materials Chemistry and Physics 240 (2020) 122160

Contents lists available at ScienceDirect

Materials Chemistry and Physics

journal homepage: www.elsevier.com/locate/matchemphys

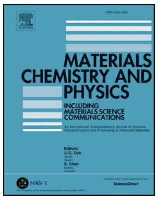

Towards high cycle stability yolk-shell structured silicon/rGO/MWCNT hybrid composites for Li-ion battery negative electrodes

Ubeyd Toçoğlu[a,*], Miraç Alaf[b], Hatem Akbulut[a]

[a] *Sakarya University, Dept. of Metallurgy and Materials Engineering, Sakarya, Turkey*
[b] *Bilecik Şeyh Edebali University, Dept. of Metallurgy and Materials Engineering, Bilecik, Turkey*

HIGHLIGHTS

- rGO/MWCNT/Si@void@C free-standing composite electrodes were prepared for the first time.
- Binder-free andfree standing electrode yields much lower electrical resistance.
- Si@void@C structure provides enough space for silicon particles to expand during lithiation without generating.
- Mechanical integrity obtained by entangled structure of rGO/MWCNT skeleton.
- rGO/MWCNT/Si@void@C electrodes have exhibited high reversible capacity and good cycle retention after 500 cycles.

ARTICLE INFO

Keywords:
Silicon
Yolk-shell
Graphene
Lithium

ABSTRACT

Owing to the highest known theoretical specific capacity of 4200 mAhg^{-1}, low lithiation voltage characteristics and natural abundance, silicon is considered as the most promising negative electrode material for lithium ion batteries which has the potential to replace graphite. Although having striking features, massive volumetric expansions leading to mechanical pulverization and unstable solid electrolyte interphase hinder silicon to be practically exploited as negative electrode material. To address this challenge we design a binder-free and free-standing composite electrode structure which contains embedded silicon yolk-shell particles between graphene/multi walled carbon nanotube skeleton as anode for lithium ion batteries. Electrochemical charge/discharge test results showed that composite anodes exhibited 951 m Ahg^{-1} of gravimetric capacity after 500 cycles. This remarkable performance could be ascribed to the complementary effect of yolk-shell particles and conductive structure of graphene/carbon nanotube skeleton.

1. Introduction

In order to reduce carbon emission levels and operational storage of electricity generated via renewable energy sources, more powerful energy storage systems in terms of capacity and efficiency are growing in importance significantly [1]. Due to increasing requirements for electric vehicles, wearable electronics and electric bicycles, development of alternative and advanced energy storage systems such as next generation lithium ion batteries, lithium sulfur batteries and supercapacitors with improved energy storage capability has attracted significant attention [3–6] Among various electrochemical energy storage technologies, Li-ion batteries (LIBs) play dominant role in day-to-day technology market for mobile power supplying, electric vehicles and large scale electrical grids owing to their high energy density, high efficiency, low self-discharge, long cycling life, low toxicity and high reliability [2]. Today's lithium ion battery technology utilizes graphite as anode material on account of its natural abundance and stable cycling performance, However, the maximum theoretical capacity of 372 mAhg^{-1} limits the production of lithium ion batteries with higher energy densities suitable for advanced applications [7]. Graphene supported metal cyanides, n- doped carbon polyhedral nanocages and metal-organic framework derived metal oxide/carbon composites are novel examples of alternative lithium ion battery anodes due to their superior specific capacity values and cycling performances compared to graphite [4,6].

Alloy-type anodes (Si, Sn, Ge, Al, etc.) have attracted tremendous interest in recent years owing to their high Li storage capacity than the intercalation-type graphite anode that is currently used in Li-ion batteries [8]. Among the all alloying type anode materials, silicon (Si) has

---

* Corresponding author.
E-mail address: utocoglu@sakarya.edu.tr (U. Toçoğlu).

https://doi.org/10.1016/j.matchemphys.2019.122160
Received 25 July 2019; Received in revised form 9 September 2019; Accepted 10 September 2019

been considered as the most promising and attractive candidate for LIBs due to its highest specific capacity ($Li_{4.4}Si = 4200\ mAhg^{-1}$) and low discharge potential (~0.5V versus Li/Li^+) [9]. Despite of these advantages, silicon anodes suffer short cycling life, as well as unsatisfactory rate-capability caused by the large volume expansion (~400%) upon insertion and extraction of lithium-ions lead to severe electrode pulverization, which results in loss of electrical contact between the active materials and the current collector, leading the rapid capacity fade [10]. Furthermore, the nonstable extend of silicon particles caused by volumetric variations leads perpetual exposure of silicon surfaces to the electrolyte that brings continual and substantial formation of very thick solid-electrolyte interphase (SEI) films which causes capacity fading and poor coulombic efficiency [11].

In order overcome these generic problems for all high capacity alloy-type anodes, much attention has been devoted to design and fabrication of the structures that have predefined void spaces and/or a conductive buffer components [12]. Silicon materials reduced from metallothermic reduction reactions (MRR) are outstanding example for silicon structures with predefined void space which might be able to stand anode pulverization. A unique advantage of MRR-formed silicon is the nano porosity, which is an intrinsic property of these materials due to its formation processes. Such emptiness inside the structures could adsorb the large volume expansion of the silicon anode during its electrochemical alloying process [13]. Thus, such porosity will be able to mitigate the pulverization of the silicon anode during operation, which enhances the cycling life. Another approach is creating Yolk-shell silicon particles of hollow and core-shell structures with a specific yolk@void@shell configuration which might be able to provide sufficient space for accommodating the volume variations of alloy type anodes during lithiation reactions [8]. Creating yolk-shell nano architectures could be very effective solution because of the void space between silicon nanoparticles and carbon coating buffers the huge volume expansion during Li^+ insertion thus preserving the integrity of the electrode framework [15]. Additionally the carbon shells provide the essential transport channels for both electrons and Li^+ from/to the inner silicon. Besides, providing space for increasing volume of silicon particles safely, carbon layer avoids the contact of electrolyte with silicon particles which ensures the formation of a homogeneous and compact solid electrolyte interphase (SEI) film on the external carbon layers surface [9, 15].

Besides this effective solution, yolk−shell structured nanoparticles/carbon composites have been produced to obtain better electrochemical properties [16]. Carbon materials such as amorphous carbon, carbon nanotubes, and graphene have been used to fabricate composite electrodes via different methods such as encapsulation, layering and binding [17]. Graphene including sp^2 hybridized carbon atoms has attracted ever−increasing attention for energy storage by reason of its two-dimensional structure, which provides about its unique mechanical, chemical, electronic, thermal, characteristics and extensive applications [18]. Despite these advantages, graphene layers tend to form irreversible aggregates during their reduction due to strong van der Waals interactions and increased hydrophobicity [19]. In order to prevent aggregation of graphene layers and increase not only interlayer distance but also surface area, combinations with various carbon materials, such as carbon nano tubes, fullerene and carbon black has been used extensively [20–22].

We report our work which aims to enhance cyclability of silicon based anodes via producing novel nano-composite electrode architecture. Although there are number of studies about silicon based yolk-shell electrodes, there is no free-standing electrode design which is composed of highly entangled graphene/carbon nanotube skeleton that contains yolk-shell silicon particles. In order to take the advantages of aforementioned precaution approaches for volume-variant alloying anodes to increase capacity and cyclability, we have designed a binder-free, free-standing Graphene/MWCNT/Yolk-Shell silicon anode structure which consists of embedded silicon yolk-shell particles between highly entangled graphene-MWCNT skeleton. Herein, graphene sheets accommodate yolk-shell silicon particles and covering them to build up a free-standing binder-free anode. Graphene covered yolk-shell particles put together an electronically contacted porous sandwich structure, thus it is anticipated that addition of carbon nanotubes renders the structure mechanically more durable to volume variations due to entanglement with graphene sheets while increasing the surface area of anode by preventing aggregation of graphene sheets. Moreover presence of carbon nanotubes in the structure enhances electrochemical performance of electrodes via reducing charge transfer resistance of values. In order to demonstrate step by step contribution of electrode components to the electrochemical performance of anode silicon yolk-shell (Si@void@C), Graphene/Silicon Yolk-Shell (rGO/Si@void@C) and Graphene/MWCNT/Silicon Yolk-Shell (rGO/MWCNT/Si@void@C) anodes have been fabricated for electrochemical characterization. The effect of mass loading of rGO and MWCNT was investigated by preparing electrodes with constant Si amount and varying MWCNT:rGO loading of 1:1, 1:2 and 2:1.

2. Experimental

rGO/MWCNT/Si@void@C free-standing composite anodes were prepared via vacuum filtration technique subsequent to graphene oxide (GO) synthesis, functionalization of multiwalled carbon nanotubes (MWCNT) and production of silicon yolk-shell particles. Thereinafter comprehensive electrode production steps and characterization procedures of study have been explained.

2.1. GO synthesis and functionalization of MWCNTs

Production procedure of free-standing rGO/MWCNT/Si@void@C composite electrodes involves couple of steps which consist of synthesizing the constituents of composite anodes. Graphene oxide was synthesized by well-known modified Hummers' method [23]. Flake like graphite (Alfa-Aesar, 100 mesh size) was subjected to two-step pre-treatment prior to the chemical oxidation in order to assure effective oxidation of graphite particles. First acidic activation of graphite surfaces was ensured via sulfuric-nitric acid solution treatment at room temperature for 2 h and a heat treatment was conducted in open atmosphere at 800 °C for 2 min in order to increase interlayer distance between graphene layers. Following the pre-treatment, modified Hummers' method was carried out. Specific amount of pre-treated graphite was added to the H_2SO_4–$NaNO_3$ solution and stirred for 2 h. The mixture then placed into the ice bath for slow addition of $KMnO_4$ for main oxidation of graphite particles [24]. After oxidation, obtained solution was washed in order to eliminate contaminations and centrifuged to collect produced graphene oxide.

Multiwalled carbon nanotubes (50–100 nm diameter range) purity up to 95% with amorphous carbon ratio of 3% were purchased from Arry Nano Materials. By the fact that production techniques of carbon nanotubes bring impurities such as Fe, Co, Ni and amorphous carbon, purification processes are necessary since they affect the properties of carbon nanotubes. Moreover carbon nanotubes have to be functionalized in order to get processsability in aqueous media by adding functional groups to the tube walls. Therefore, purification and functionalization steps applied to as received carbon nanotubes which were well described in our previous study [25].

2.2. Production of yolk-shell silicon particles

Pulverization that arisen from volumetric variation and direct contact of silicon surfaces to the electrolyte are two main challenges which are harshly in the way of silicon anodes commercialization. Sufficient and well-distributed porosity in silicon based anodes to accommodate volume expansion with stable SEI layer is the key to successful design for long cyclability [8]. Nano sized "Yolk-Shell" architecture is a promising structure since it takes into account several precautions in order to prevent above mentioned failure mechanisms of silicon based lithium ion battery electrodes. It provides free space to accommodate volumetric expansions between silicon yolk and carbon shell while carbon shell prevents direct contact of silicon particle surfaces to the electrolyte which causes consumption of electrolyte due to formation of unstable SEI layer. In this study, we have synthesized silicon yolk-shell structure that has 50–100 nm sized silicon particles as "Yolk" and amorphous carbon as "Shell" with 5–10 nm thickness. Preparation steps and schematic representation of yolk-shell silicon structure is shown at Fig. 1.

As it is presented at the schematic illustration, yolk-shell preparation has three basic steps that involves silica coating process, carbon coating process by resorcinol-formaldehyde resin (RF) coating and finally hydrofluoric acid (HF) etching of silica sacrificial layer. As-received silicon nano particles between 50 and 150 nm were coated with silica layer according to Stöber sol-gel method that composed of hydrolysis of tetra ethyl ortho silicate (TEOS) and polycondensation of silica (SiO_2) reactions [9]. By the contact of silicon particles to the open atmosphere a thin layer of silica gets formed on the silicon particle surfaces which behaves as nucleation sites for SiO_2 growth at the Stöber process. Silica formation takes place on silicon surfaces via adding proper TEOS concentrations with proper rates according to given equations below.

$$Si(OC_2H_5)_2 + 4H_2O \rightarrow Si(OH)_4 + 4C_2H_5OH \text{ (Hydrolysis, pH: 10–12)} \quad (1)$$

$$Si(OH)_4 \rightarrow SiO_2 + 2H_2O \text{ (Polycondensation, pH: 10–12)} \quad (2)$$

The silica coating was performed in a dispersion that contains absolute ethanol (240 mL) and distilled water (60 mL). Prior to the TEOS introduction into the solution, silicon nano particles (150 mg) were dispersed in an ethanol-water solution under ultrasonic agitation for 1h with the presence of hexadecyltrimethylammonium bromide (CTAB) in order to obtain well dispersion. After ultrasonication, ammonia solution (25%) was added as catalyst for Stöber process reactions until adjusting pH range of dispersion to the 10–12 levels. Under vigorous magnetic stirring, TEOS (6 mL) was added to the dispersion dropwise in 1h and was stirred for additional 6h at 25 °C in order to complete formation and growth of SiO_2 layer. Finally, dispersion was centrifuged and washed with ethanol several times to collect core-shell SiO_2 coated silicon nanoparticles ($Si@SiO_2$). Carbon coating of $Si@SiO_2$ particles was carried out in a tubular furnace under argon atmosphere at 900 °C for 2 h subsequent to RF resin coating on $Si@SiO_2$ nano particle surfaces. The typical resorcinol formaldehyde coating process could be simply described as polycondensation reactions of resorcinol with formaldehyde in a water and ethanol containing solution [26]. Fang and Coworkers have demonstrated that hexadecyltrimethylammonium bromide is crucial for RF resin coatings of SiO_2 surfaces since the low concentration of formaldehyde and resorcinol could not finally yield to a RF resin coating layer on the surfaces in the absence of CTAB. It is well known that CTAB has affinity to SiO_2 surfaces in basic medias and encourages the condensation reactions of resorcinol and formaldehyde at the surfaces of SiO_2 with low concentrations [27]. Therefore, in order to synthesis $Si@SiO_2@RF$ structures we have prepared a dispersion of 150 mg of $Si@SiO_2$ particles under ultrasonic agitation for 0.5 h in a solution containing 50 mL of absolute ethanol, 50 mL of distilled water, and 200 mg of CTAB. After sonication, 30 mg of resorcinol and 0.2 mL of formaldehyde solution was introduced to the dispersion and ultrasonicated additional 0.5 h. Finally 3 mL of ammonia solution was added to the dispersion and left for stirring at 35 °C for 12 h. In the end of the RF resin coating process, $Si@SiO_2@RF$ particles were collected and washed with ethanol via vacuum filtration. Afterwards, obtained product was placed in a tubular furnace at 900 °C with the heating rate of 10 °C/min. for 2 h under argon atmosphere to conduct carbonization of RF resin coating layer. After furnace was cooled down to room temperature, carbon coated particles which are symbolized as $Si@SiO_2@C$ were selectively etched in 5% HF solution in order to discard sacrificial SiO_2 layer to finally obtain silicon yolk-shell (Si@void@C) structures. In the sequel of 15 min of HF etching, obtained product was washed with distilled water several times until pH value of 6 was achieved and dried in vacuum oven at 50 °C for 24 h.

2.3. *Preparation of rGO/MWCNT/Si@void@C free-standing composite anodes*

Fig. 2 shows the schematic illustration of free-standing anode production. It was purposed to obtain highly entangled rGO-MWCNT skeleton layers with the yolk-shell particles inserted between, thus steps were followed as it is described below. Under the favor of hydrophilic nature of graphene oxide and functionalized carbon nanotubes it is easy to exfoliate them by means of ultrasonic agitation in an aqueous media [28].

Therefore, in order to build up the structure of rGO/MWCNT/Si@void@C free-standing composite anodes, certain amount Si@void@C particles were used with the weight ratio MWCNT:GO of 1:1, 1:2 and 2:1. Graphene oxide sheets and carbon nanotubes first dispersed in water by the ultrasonic agitation. For supplying the highest level exfoliation of graphene oxide sheets, pH value was adjusted to 10 by means of adding ammonia solution to the dispersion. After 0.5 h ultrasonic process of GO-MWCNT dispersion, yolk-shell silicon particles were introduced in company with CTAB which provides breaking the bundles of yolk-shell silicon particles. Hydrazine hydrate solution was

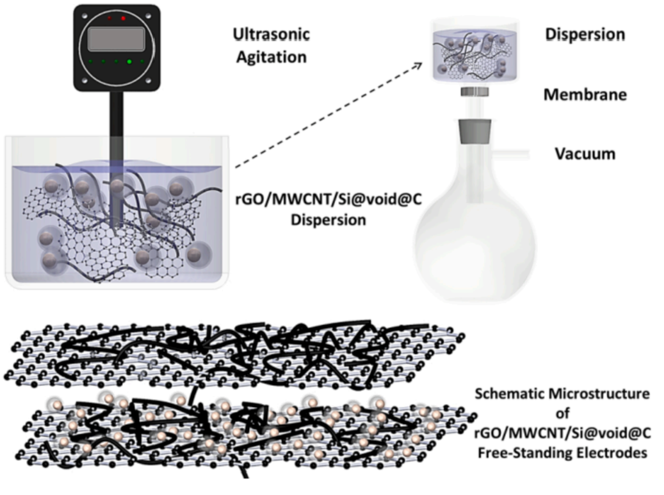

Fig. 2. (a) Schematic illustration of preparation and structure of rGO/MWCNT/Si@void@C free-standing composite anodes.

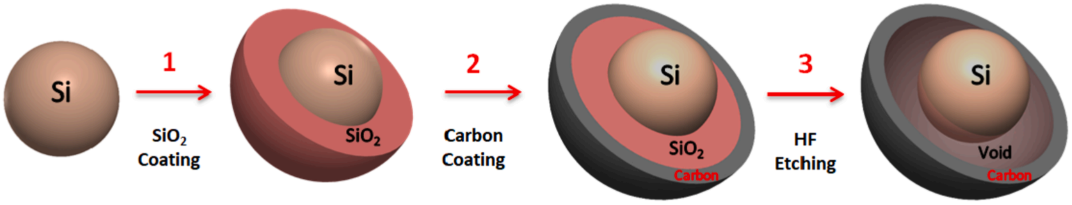

Fig. 1. The Schematic illustration of yolk-shell structured particle synthesis.

added to the dispersion after 0.5 h of ultrasonication in order to reduce graphene oxide to graphene and sonication was conducted 1.0 h more. At the end of the process, dispersion was vacuum filtered through the 220 nm pore sized PTFE membrane, washed with distilled water, dried under vacuum at 50 °C for 24 h and free-standing anodes were handled by peeling off from membranes.

2.4. *Phase and morphological characterization*

Crystal structure and phase constituents of samples were characterized by X-Ray diffraction (XRD) analysis technique using a RIGAKU D/MAX 2000 X-ray diffractometer with CuKα ($\lambda = 1.54056$ Å) radiation. The diffraction patterns were registered in the step scan mode, with a beam incidence angle of 0.5°, and recorded at 2° (2θ) steps with a constant time of 1 min per step in the range $10^\circ < 2\theta < 90^\circ$. Further phase analyses of products were performed by means of RAMAN spectroscopy technique with a KAISER Raman Rxn system with laser wavelength of 712 nm. To determine the mass ratio of silicon in Si@void@C and rGO/MWCNT/Si@void@C structures thermogravimetric analyses (TGA) were performed with a NETZSCH DTA-TG thermal analysis system under oxygen atmosphere up to 1000 °C with heating rate of 10 °C/min. Morphological characterizations were performed by scanning electron microscopy (FEI, Quanta FEG 450) and transmission electron microscopy (Jeol JEM2100F) techniques. The elemental mapping analysis was carried out by an energy-dispersive X-ray spectrometry (EDS, Edax Octane Elect Plus).

2.5. *Electrochemical characterization*

All electrochemical measurements were performed by utilizing standard CR2016 coin cells. Coin cells were assembled in an argon filled glovebox (MBRAUN) employing lithium foil as counter electrode and 1 M $LiPF_6$ in ethylene carbonate/dimethyl carbonate (1:1) as the electrolyte (0.40 mL). For galvanostatic charge/discharge tests rGO/MWCNT/Si@void@C, rGO/Si@void@C free-standing electrodes (7.5 mg) and Si@void@C PVDF-NMP slurry electrodes (15 mg) were prepared as working electrodes. Galvanostatic charge/discharge tests were carried out at a potential window of 0.01–1.5 V with constant current density of 200 mAg^{-1} by a MTI BST8-MA Battery analyzer. Cyclic voltammetry (CV) tests were performed in the potential window of 0.01–2V at a scanning rate of 0.25 mVs^{-1} via electrochemical work station (Gamry Instruments Reference 3000). Electrochemical impedance measurements were performed at frequency range from 1000 kHz to 0.1 Hz in order to achieve data about resistance of cells.

3. Results and discussion

Fig. 3 shows as prepared electrodes and a cross-sectional SEM image. rGO/MWCNT/Si@void@C free-standing composite electrodes were successfully handled after drying overnight at vacuum oven and peeling-off from membranes. Electrodes were able to be flexibly folded like a paper without any failure. Preliminary SEM examination proved that purposed structure of silicon yolk shell particles that are covered by highly entangled graphene sheets and carbon nanotubes was obtained.

XRD analyses were carried out to verify the crystalline structure of products of whole anode production process of the study. The XRD spectrum of rGO (Fig. 4a) shows broad a peak centered around $2\theta = 25^\circ$ indicates amorphous atomic structure of graphite [29]. Moreover, $Si@SiO_2@C$, Si@void@C and rGO/MWCNT/Si@void@C samples have broad reflections around $2\theta = 20\text{-}30^\circ$ (Fig. 4b) that indicates amorphous carbon structure [11]. The sharp peak appeared at $2\theta = 26.14^\circ$ (002) in the pattern of rGO/MWCNT/Si@void@C exhibited by (002) reflections of multiwalled carbon nanotubes [30]. Except that of graphene, all samples exhibit same reflection patterns of silicon crystalline structure located at $2\theta = 28.5^\circ$, 47.4°, 56.2°, 69.2°, 76.4°, 88.1° correspond to the (111), (220), (311), (400), (331), (422) planes, respectively [31].

However, decrement at the intensities of silicon reflections could be deduced as decreasing ratio of silicon phase of the samples which could be verified by TGA analysis either. No other reflections were observed other than main constituents which could be ascribed to no residual SiO_2 phase after etching the sacrificial layer or formation of other chemical by-products.

In order to acquire more information about structure of rGO/MWCNT/Si@void@C anodes RAMAN spectroscopy analyses were conducted to rGO/MWCNT/Si@void@C and rGO samples. The results are presented at Fig. 4c shows strong peaks at 520 cm^{-1} and 932 cm^{-1} that could be ascribed to first order TO and second order 2TO phonon scatterings of crystalline silicon which are characteristic for RAMAN spectrum [32]. D-band at the 1320 cm^{-1} is related to the disordered defect structure of sp^3 electronic vibrations of carbon materials. G-band at 1590 cm^{-1} is ascribed to graphitic structure of sp^2 bonded carbon atoms. G^I-band appears around 2700 cm^{-1} is an overtone of D-band that is related to the sp^2 graphitic bonds. The difference at intensity of G^I band is related with the existence of carbon nanotubes since ordered carbon structures such as carbon nanotubes shows more intensive G^I peaks compared that of reduced graphene oxide [33]. D, G and G^I bands are all characteristic for RAMAN spectrum of carbon structures including amorphous carbon, rGO and carbon nanotubes which are constituents of rGO and rGO/MWCNT/Si@void@C samples that contribute to the finding of XRD results.

Chen and co-workers have reported that the intensity ratio of D and G bands (I_D/I_G) could be used to evaluate separation level of graphene

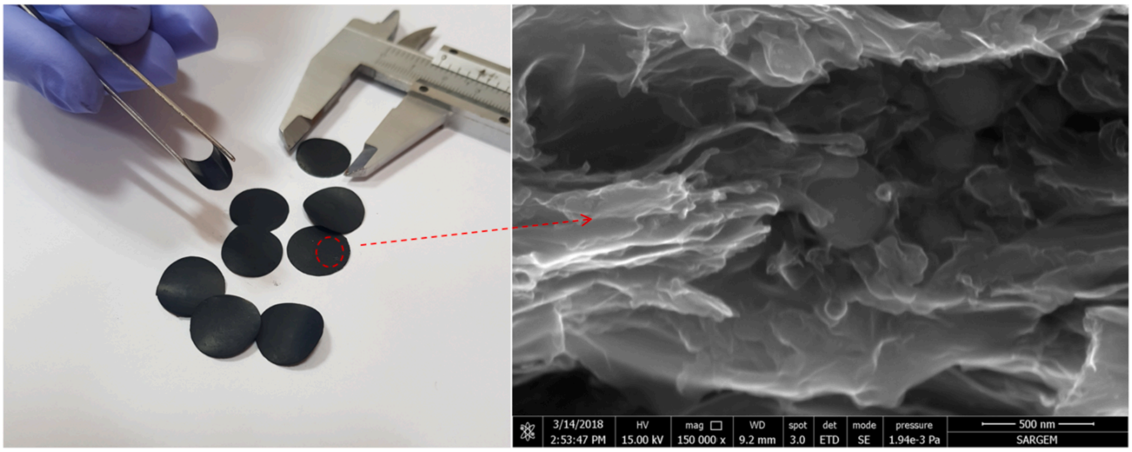

Fig. 3. rGO/MWCNT/Si@void@C free-standing composite electrodes and a cross-sectional SEM image.

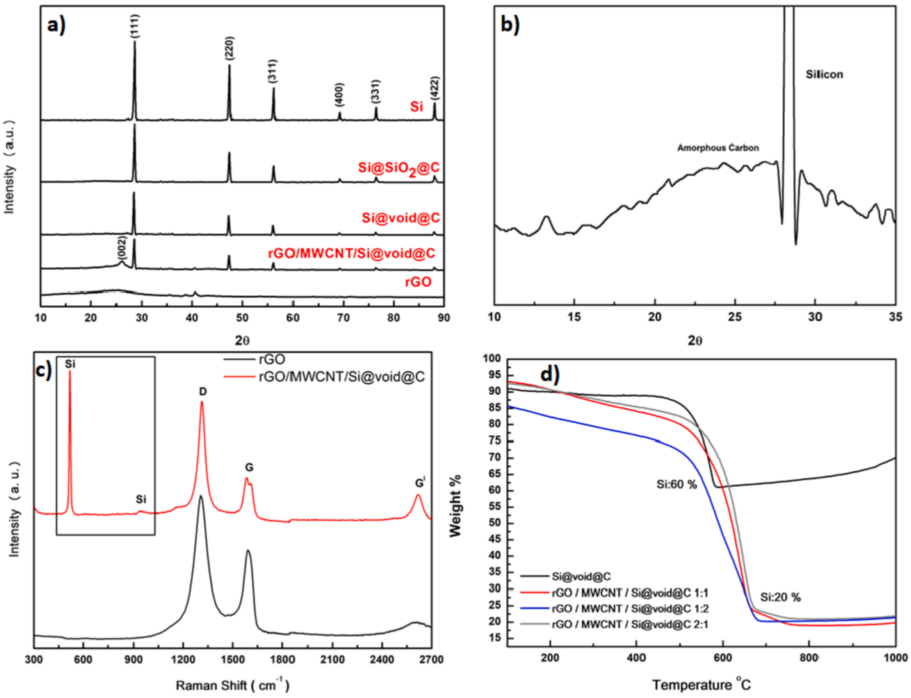

Fig. 4. (a) XRD patterns of Si, rGO, Si@SiO$_2$@C, Si@void@C and rGO/MWCNT/Si@void@C, (b) narrowed spectrum for amorphous carbon pattern, (c) Raman spectroscopy analysis of rGO and rGO/MWCNT/Si@void@C electrode samples, (d) TGA analysis of Si@void@C and rGO/MWCNT/Si@void@C samples.

sheets since the D band is related to the defects and disordered carbon structure while G band is related to the ordered sp^2 C–C bonds [34]. Moreover Xing et al. have reported the lower I_D/I_G and presence of 2D band indicates limited population of defects in graphene sheets [35]. In comparison with their study I_D/I_G ratio is much higher due to the hydrazine reduction of graphene oxide sheets which yields more defective graphene structure. The I_D/I_G ratios were calculated as 1.57 and 2.15 for rGO and rGO/MWCNT/Si@void@C samples respectively. It could be concluded that introduction of carbon nanotubes and yolk-shell particles into the anode structure, has prevented the agglomeration by settling down between graphene layers which is favorable to the electrode performance due to the increment of surface area [36]. Also coherence length along ab planes (graphenic layers) is quantitatively correlated to the I_D/I_G according to following equation [37,38];

$$L_a\ (nm)\ = (2.4\cdot10^{-10})\cdot\lambda_{nm}^{4}\left(\frac{I_G}{I_D}\right) \tag{3}$$

where λ is 712 nm of laser. According to equation coherence length of reduced graphene oxide was calculated as 39, 43 nm indicating there are plenty of defective graphenic domains.

TGA analysis was performed in order to determine the weight percentage of silicon at Si@void@C and rGO/MWCNT/Si@void@C anode samples (Fig. 4d). Analyses were conducted under air flow up to 1000 °C. The weight losses before 500 °C were caused by removal of adsorbed water and pre-decomposition of carbon. After 500 °C carbon content of samples was oxidized completely reached up to 650 °C [11]. In addition, anode with 1:2 MWCNT:rGO weight ratio got oxidized faster than other two anodes indicating the lower thermal stability of reduced graphene oxide compared to the carbon nanotubes. According to the TGA curves, weight ratio of silicon could be calculated as 60% for Si@void@C sample and 20% for all rGO/MWCNT/Si@void@C composite anodes.

At the first step of Si@void@C preparation, surfaces of commercially available silicon nanoparticles ranging from 50 nm up to 150 nm (Fig. 5a) were coated with SiO$_2$ via hydrolysis of TEOS (Fig. 5b). SiO$_2$ layer could be easily observed by the increased size of silicon nanoparticles.

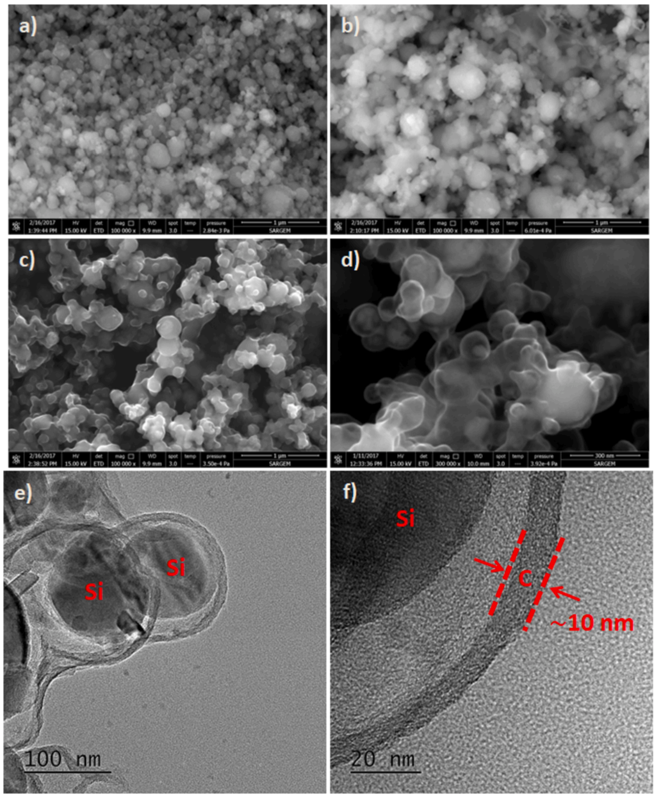

Fig. 5. SEM images of (a) bare nano silicon particles, (b) Si@SiO$_2$ particles, (c) Si@SiO$_2$@C particles, (d) Si@void@C particles, (e) and (f) TEM image of Si@void@C particle.

Carbon coating process of Si@SiO$_2$ composite particles was carried out via carbonization of.

Moreover CTAB transforms into carbon during high temperature carbonization and builds pores on the carbon layer which enhances ionic Li transportation [39]. Si@void@C yolk-shell structures were observed (Fig. 5 d) after selective etching of silica layer by HF solution treatment. For further validation and detailed visual information of yolk-shell structure TEM analysis was employed (Fig. 5 e, f). The structure consists of an amorphous carbon "*shell*" with thickness of 5–10 nm which encapsulates the silicon nano particle as a "*yolk*" while there is aplenty of void space between carbon layer and silicon nano particle. All individual yolks are in contact with carbon shell which ensures the ion/electron transportation during electrochemical reactions. Such yolk-shell structures have several advantages in terms of improvement of cycling performance of aggressively volume variant alloying anode materials like silicon. First and the foremost, the void between carbon shell and silicon yolk provides the adequate free space for expansion of silicon nano particles during lithiation that prevents the mechanical failure of silicon particles. Even if the pulverization of silicon nanoparticles occurs, carbon shell would keep the pulverized fragments together thus prevents relatively rapid capacity loss compared that of classic silicon anode structures. The other beneficial feature of yolk-shell structure is to keep silicon nano particles away from direct contact with electrolyte which results in degradation of electrolyte with the continual formation of SEI layer on the particle surfaces due to astatic volume during lithium insertion/extraction processes. Yolk-shell structure provides a stable SEI layer growth on the static carbon layer at the initial cycles which in turns prevents the capacity losses due to the electrolyte degradation [8,40].

Cross-sectional SEM images and elemental EDS map analysis results of rGO/MWCNT/Si@void@C free-standing composite anodes which were prepared by vacuum filtration after yolk-shell production are shown in Fig. 6. Results have revealed that anodes were fabricated with 80 μm thickness (Fig. 6a) and uniformly distributed rGO/MWCNT layers. No defects were observed along the cross section, rGO/MWCNT packaging has yielded a laminar-porous skeleton structure that could behave as a mechanical cage for Si@void@C particles.

Higher magnification SEM images of rGO/MWCNT/Si@void@C electrode, shown in Fig. 6b indicates morphology of Si@void@C particles covered by a homogenous, highly entangled cage-like porous rGO/MWCNT network. Introduction of MWCNTs between rGO layers expands interlayer spacing of graphene sheets that significantly enhances the pore distribution and surface area of structure which was also reported by Wimalasiri and co-workers [19]. Elemental mapping analysis shows carbon and silicon distribution along the cross section of electrode (Fig. 6c and d). Homogenous carbon and silicon signal indicates the well distribution of Si@void@C particles between rGO/MWCNT skeleton.

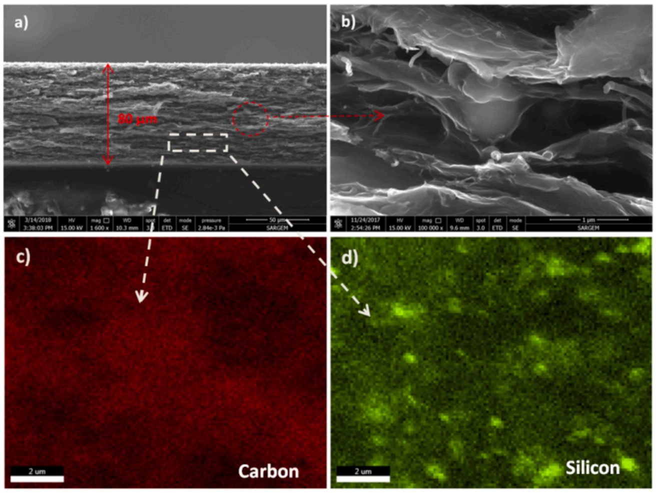

Fig. 6. Cross sectional SEM images of rGO/MWCNT/Si@void@C electrodes. (a) lower magnification, (b) higher magnification, (c) and (d) cross sectional EDS map analysis of electrodes.

The pore size distribution and surface area both have very important roles in electrochemical performance, higher surface area and mesoporous structure derives shorter lithium ion diffusion pathways and less electrical resistivity as well as increased accessible electrochemical-active areas for lithiation processes. MWCNT introduction into the graphene sheets offers the enhancement of electrode performance by means of decreasing electronic resistivity since it has lower resistance than graphene. Moreover spacer role of carbon nanotubes for graphene layers results with higher ionic accessibility [41,42]. Therefore it's expected to obtain higher specific capacity and enhanced cycle performance from rGO/MWCNT/Si@void@C electrodes than those of rGO/Si@void@C composite electrodes. Beside the improvement of electrochemical characteristics of anodes, mechanical durability is the key factor for cyclability. Our novel micro structural design embodies several mechanical precautions for failures caused by stress induced mechanical disintegration. As it is clear from Fig. 5d silicon particles are covered by void space which host volume increments and prevent anode from mechanical failure. However, in case of a number of yolk-shell particles having insufficient void space, amorphous carbon layer of yolk-shell particles and rGO/MWCNT layer could hold the structure together with their extraordinary mechanical strengths. As it is presented at Fig. 6b, Si@void@C particles are covered by highly entangled rGO/MWCNT sheets and it's expected that buffering effect of rGO/MWCNT composite layers would suppress the volume increment of silicon particles while preventing anode from total volume increment and disintegration.

The electrochemical tests were conducted with assembled coin type CR2016 cells using lithium foils as counter electrode and rGO/MWCNT/Si@void@C electrodes as working electrode. Cellgard membrane (PP) was used as separator and 1 M $LiPF_6$ salt dissolved in ethylene carbonate (EC)-dimethyl carbonate mixture was used as electrolyte. All galvanostatic charge/discharge tests were conducted between voltage range of 0.01–1.5 V with 200 mAg^{-1} constant current density. Cyclic voltammetry test of rGO/MWCNT/Si@void@C electrodes were performed between voltage ranges of 0.01–2 V at 0.25 mVs^{-1} sweep rate. Fig. 7 shows typical cyclic voltammetry plots for first two cycles and galvanostatic charge/discharge profiles of rGO/MWCNT/Si@void@C composite anodes between 0.01 and 1.5 V for 1st, 2nd, 50th, 200th and 500th cycles.

At first CV cycle of all samples, broad peaks appear between 1.2-1.5 V and 0.15–0.5 V in the cathodic branch of curve which corresponds to the formation of solid electrolyte interphase arisen from decomposition of electrolyte [32]. The reduction peak of SEI formation disappears at following cycle indicating the stable SEI layer formation. As sweep goes to lower potential values, a sharp peak appears at~0.2 V of cathodic branch which is attributed to formation of amorphous Si–Li phase and the peaks at 0.35 V and 0.5 V at the anodic part of the curve correspond to the extraction of Li^+ from Li–Si alloy phases [43,44]. It should be noted that sharpness of peaks has exhibited an increasing pattern with the increasing MWCNT ratio at the anode composition. The rGO/MWCNT/Si@void@C anode with 2:1 wt ratio of MWCNT:rGO has presented highest current intensity at the CV plots which could be evaluated as higher electrochemical activity due to the improving electrode kinetics by means of decreasing electrical and ionic resistance of anode.

Capacity values were calculated according to total electrode weights and the applied current density was 200 mAg^{-1}. A long and flat discharge plateau was observed in the first cycle of charge/discharge tests (Fig. 7a, b, 7c) which is attributed to formation of SEI on the surface of the electrode that shows consistency with CV test results. This occurrence was not observed at following cycles since the SEI structure was maintained without damage that is also has agreement with CV result. At the initial cycle, rGO/MWCNT/Si@void@C composite anodes with MWCNT:rGO ratios of 1:1, 1:2, 2:1 has exhibited 2560 $mAhg^{-1}$,

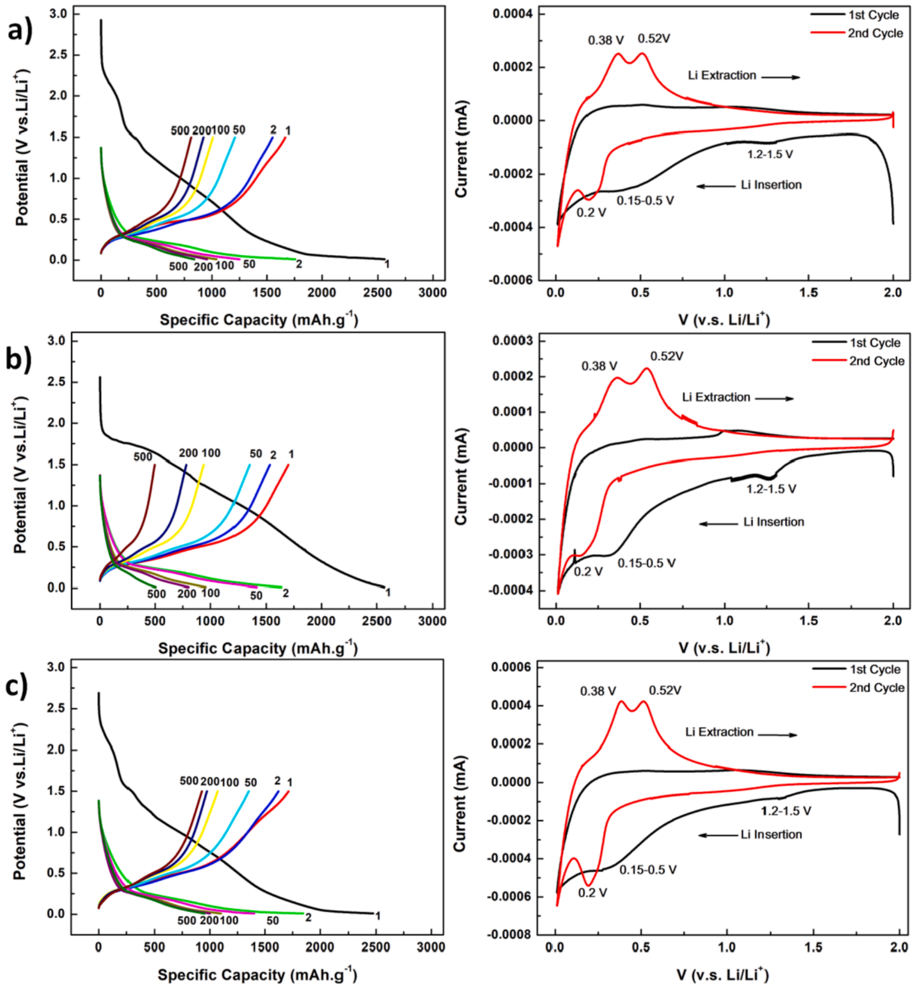

Fig. 7. Galvanostatic charge/discharge profiles and Cyclic voltammetry diagrams of rGO/MWCNT/Si@void@C composite electrodes with MWCNT:rGO ratio of (a) 1:1, (b) 1:2, (c) 2:1 respectively.

2562 mAhg^{-1} and 2472 mAhg^{-1} discharge capacity values respectively. At the second cycle of test, anodes possess 1755 mAhg^{-1}, 1532 mAhg^{-1} and 1621 mAhg^{-1} of discharge capacity values at same order of MWCNT: rGO ratios. Discharge curves exhibits sloping potential plateau at 0.2 V that corresponds to lithiation of silicon. The charge plateaus at 0.3 V and 0.5 V values ascribed to the lithium ion extraction process from silicon [45]. After 100 cycles discharge curves starts to get closer implying lower capacity loss with more stable electrochemical processes. After 500 cycles with current density of 200 mAhg^{-1} rGO/MWCNT/Si@void@C electrodes has exhibited 820 mAhg^{-1}, 503 mAhg^{-1} and 951 mAhg^{-1} of discharge capacity value. With accordance of data acquired from CV results that highlights higher MWCNT loading leads up better electrochemical activity, similar result was obtained from galvanostatic charge/discharge tests. Anode which has 2:1 MWCNT:rGO loading has exhibited the highest specific capacity and capacity retention value of 52% compared to anodes with 1:1 and 1:2 of 45% and 30%. The higher performance of anodes with 2:1 ratio is a result of combined contribution of MWCNTs on mechanical integrity and electrochemical activity.

The galvanostatic charge/discharge performance comparison diagram of all rGO/MWCNT/Si@void@C, rGO/Si@void@C and Si@void@C anodes between 0.01 and 1.5 V with current density of 200 mAhg^{-1} for 500 cycles is presented at Fig. 8a. The initial discharge capacity values exhibited by anodes were measured as 3300 mAhg^{-1}, 2700 mAhg^{-1}, 2560 mAhg^{-1}, 2562 mAhg^{-1} and 2472 mAhg^{-1} for Si@void@C, rGO/Si@void@C and rGO/MWCNT/Si@void@C with 1:1, 1:2 and 2:1 respectively. Si@void@C anode showed the higher specific capacity values at the beginning of test since it has higher silicon loading compared of other type of electrodes. Despite of higher specific discharge capacity values of Si@void@C anodes, the capacity fade occurs faster than other two electrodes due to insufficient mechanical stability. As it was mentioned, yolk-shell structure could be able to provide void space for volume expansion of silicon during lithiation when it is assumed that all yolk-shell particles have enough void volume to accommodate volumetric variations. In fact, it is expected that there are number of yolk-shell particles that could not provide enough space for huge volume expansion of silicon which is possibly responsible of capacity fade originated from partial disintegration of anode. Si@void@C electrode has exhibited 320 mAhg^{-1} of specific capacity with 15% capacity retention after 500 cycles which is quite lower than composite electrodes.

rGO/Si@void@C and rGO/MWCNT/Si@void@C (1:1, 1:2, 2:1 MWCNT:rGO) freestanding composite electrodes have exhibited 500 mAhg^{-1}, 820 mAhg^{-1}, 503 mAhg^{-1} and 951 mAhg^{-1} specific discharge capacity values respectively after 500 cycles. At second cycle the delivered specific reversible discharge capacities was found to be as 1650,1755, 1532 and 1621 mAhg^{-1} for rGO/Si@void@C and rGO/MWCNT/Si@void@C anodes. MWCNT presence in the structure provides more efficient ionic and electronic conductivity by reducing electronic resistance. Moreover the MWCNT derives easier ionic accessibility to the Si@void@C particles by splitting graphene stacks up. As well as higher specific capacity values achieved by rGO/MWCNT/

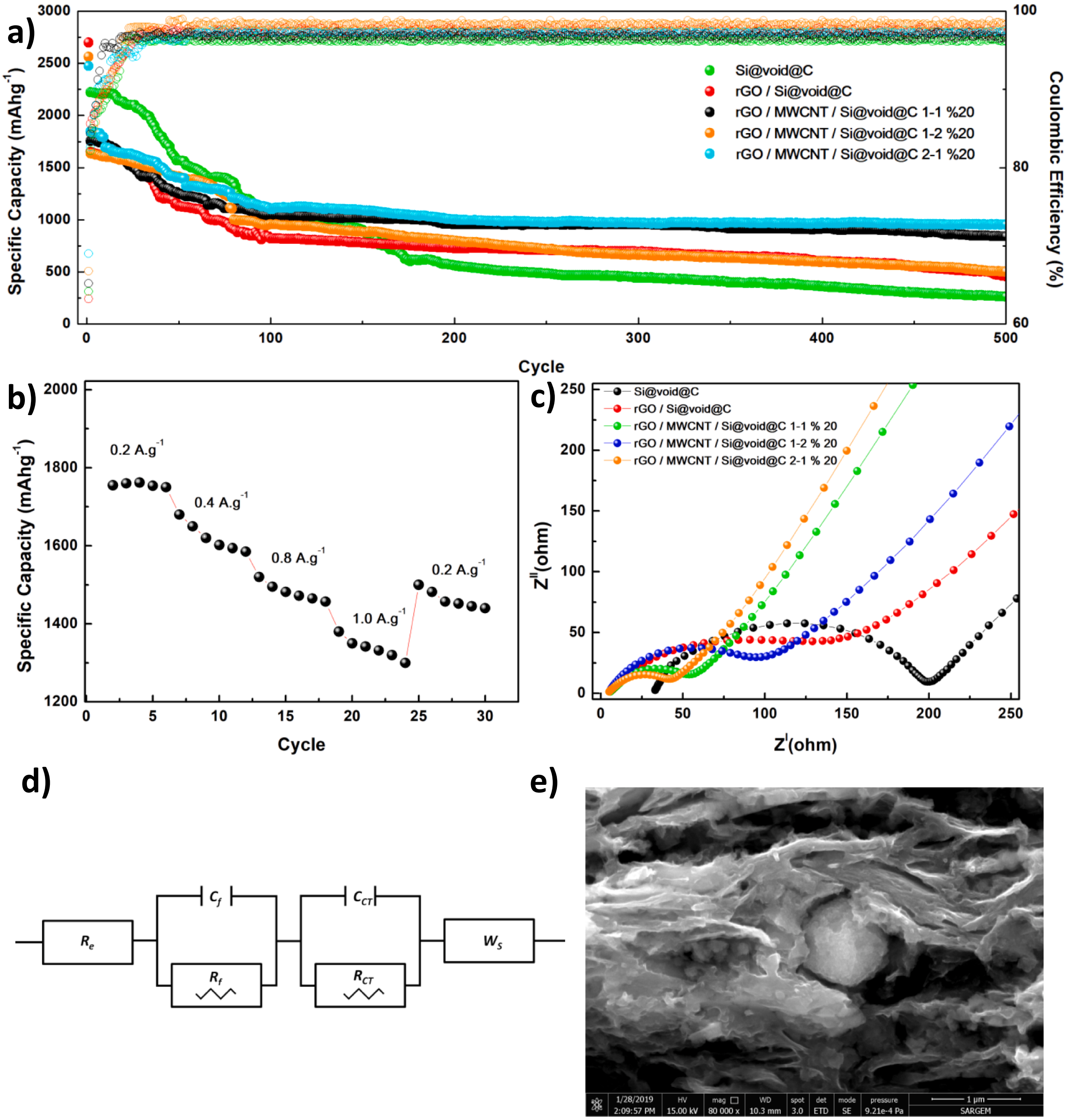

Fig. 8. (a) cycling performance and coulombic efficiency diagram of rGO/MWCNT/Si@void@C, rGO/Si@void@C and Si@void@C electrodes, (b) rate capability performance between 0.2 and 1.0 Ag^{-1} current densities (c) electrochemical impedance spectroscopy data of rGO/MWCNT/Si@void@C, rGO/Si@void@C and Si@void@C electrodes, (d) corresponding equivalent circuit for cells, (e) cross-sectional scanning electron microscopy image of rGO/MWC NT/Si@void@C anodes after 500 charge/discharge cycles.

Si@void@C structure, the capacity retention ability was found to be much better compared that of rGO/Si@void@C anodes due the MWCNT reinforcement provides higher mechanical integrity to anode by constructing a entangled cage-like structure.

Results of cyclic performance comparison revealed that the capacity retention ability of Si@void@C anodes has significantly improved by constructing free standing rGO and rGO/MWCNT reinforced anodes over the previous reports [46]. Attention should be paid on the point that rGO/MWCNT/Si@void@C composite electrode with 2:1 MWCNT: rGO loading has stopped losing its capacity after 500 cycles indicates the prescience could be made that electrode has reached to its stable capacity values and would exhibited almost same capacity at prolonged galvanostatic charge/discharge cycles. Fig. 8a also represents coulombic efficiencies of all electrodes prepared for the study. The initial coulombic efficiency values were calculated approximately 65% which is low yet common for lithium ion batteries due to the solid electrolyte interface formation at first discharge which yields lithium ion consumption and so low coulombic efficiency. However at subsequent cycles coulombic efficiency values have risen to the range of 96–98% without significant difference suggests all anode types exhibited good cycling stability.

rGO/MWCNT/Si@void@C free-standing composite electrode with 1:1 MWCNT:rGO ratio was subjected to galvanostatic charge discharge test at higher current densities. As shown in Fig. 8b, the cell was tested at a current density of 0.2 Ag^{-1} for five cycle and then 0.4, 0.8 and 1.0 Ag^{-1} current densities applied for each five cycles. The capacity values obtained for each increasing stage of current density was measured as 1585, 1457 and 1300 $mAhg^{-1}$. Remarkably, the reversible capacity value delivered by composite electrode at current density of 0.2 Ag^{-1} was recovered to the 1440 $mAhg^{-1}$ that indicates the good rate capability of electrode. The satisfying rate capability of electrode could be dedicated to the superior electrical conductivity of composite structure which is provided by excellent structure of rGO/MWCNT combination.

Potentiostatic electrochemical impedance spectroscopy measurements were carried out for Si@void@C, rGO/Si@void@C and rGO/MWCNT/Si@void@C electrodes before cycling in order to verify our claims about conductivity of electrodes that has role in terms of improved electrochemical performance (Fig. 8c). Fig. 8d shows modified equivalent circuit model used for obtaining key parameters from impedance analysis. R_e equivalent cell component represents the total resistance of cell constituents such as separator, electrolyte and electrodes. R_e values were measured almost similar for composite electrodes (5.42 Ω, 4.49 Ω, 4.46 Ω for 1:1, 1:2, 2:1 MWCNT:rGO respectively) due to same free-standing anode preparation method and anode ingredients. However, R_e value of Si@void@C anode was measured much higher (31.92 Ω) which could be ascribed to electrode prepared with PVDF has higher contribution to the bulk resistance of cell than binder free electrodes. Nyquist plots have a depressed semicircle at high-frequency zone of plot and an inclined line at the low-frequency zone of plots which represents charge transfer (R_{CT}) resistance of cell and ion diffusivity (W_s) respectively [47]. The highest semicircle diameter belongs to Si@void@C anode since it has the highest charge transfer resistance (165.5 Ω) since it has worse kinetic characteristic compared to composite electrodes. On the other hand, rGO/Si@void@C (R_{CT}: 110,7 Ω) and rGO/MWCNT/Si@void@C free standing electrodes ($R_{CT:}$ 79,9 Ω, 53,46 Ω, 37,94 Ω for 1:1, 1:2, 2:1 MWCNT:rGO respectively) have shown much smaller semicircle diameters because of binder free preparation method. Moreover, with significantly low electronic resistance, graphene addition has another contribution to lowering internal charge transfer resistance of rGO/Si@void@C electrodes. R_{CT} values are in accordance with previous discussions of paper that MWCNT addition enhances electrochemical performance by means of reducing the charge transfer resistance, increasing electronic and ionic conductivity. As it could be deduced from R_{CT} values obtained from fitting of equivalent circuit to the impedance analysis rGO/MWCNT/Si@void@C free-standing electrodes have the smaller semicircle diameter that implies addition of MWCNT has lowered the internal resistance [41,42]. On other hand, comparison of the R_{CT} values of rGO/MWCNT/Si@void@C anodes with different MWCNT:rGO loading shows the increasing content of MWCNT has resulted to lower charge transfer resistance values that explains better electrochemical performance of rGO/MWCNT/-Si@void@C anode with 2:1 MWCNT:rGO loading. Moreover the slope of the line in the low frequency region increases that implies higher lithium ion diffusivity with increasing MWCNT content.

Cells were disassembled in order to analyze morphology changes of rGO/MWCNT/Si@void@C structure after galvanostatic cycling. Fig. 8d presents cross sectional SEM image of composite electrodes after 500 cycles at fully delithiated state. It can be seen that SEI film has been formed at the surfaces of rGO sheets, MWCNTs and carbon shell after cycling. rGO/MWCNT/Si@void@C structure could be able to keep its laminated structure that holds yolk-shell particles without cracking and fracture. Figure represents a silicon particle still remains encaged in an amorphous carbon shell which is semi-intact; however it should be noted that carbon shell might be broken during preparation of sample for cross sectional SEM analysis since the half of the carbon shell still remains undistorted. Moreover it was mentioned previously on paper that a number of yolk-shell particles would be damaged due to insufficient empty space between silicon yolk and carbon shell and even so rGO/MWCNT skeleton would keep them together without failure that might cause loss of electrical contact and continuous SEI formation.

Briefly, electrochemical performance improvement could be dedicated to several features that have been achieved by our novel anode architecture as it follows: (1) binder-free free standing electrode yields much lower electrical resistance and eliminates failures such as delamination, loss of electrical contact with current collector …, (2) Si@void@C structure provides enough space for silicon particles to expand during lithiation without generating stress along entire electrode. (3) mechanical integrity obtained by entangled structure of rGO/MWCNT skeleton provides buffering effect of yolk-shell particles which have insufficient void space for volumetric variations. Thus if a yolk-shell particle is in the tendency of breakdown rGO/MWCNT holds structure together and prevents failure of particle. (4) The amorphous carbon layer prevents silicon particles direct contact from electrolyte which results with continuous degradation of electrolyte thus irreversible capacity loss. (5) Carbon nanotubes lower electrochemical resistance and add additional surface area that maintains better electrochemical kinetics by means of increasing electrical and ionic conductivity.

4. Conclusions

In the view of data obtained from structural and electrochemical measurements, it could be concluded that a significant performance improvement was achieved in terms of capacity retention and energy density for silicon based lithium ion battery anodes by synergistic effect of composite anode constituents. In summary, we have developed an anode structure in order to enhance the performance of silicon based lithium ion batteries. For preparation of anodes yolk-shell silicon particles (Si@void@C) were synthesized. In order to build composite structure reduced graphene oxide was synthesized by modified Hummers' method and multiwalled carbon nanotubes were functionalized. rGO/MWCNT/Si@void@C free-standing composite electrodes were prepared via vacuum filtration. Electrochemical performance tests showed that with composite structure, higher capacity values (951 $mAhg^{-1}$) were achieved compared that of many yolk-shell silicon study reports.

Acknowledgement

This work is supported by the Scientific and Technological Research Council of Turkey (TUBITAK) under the contract number 214M125. The authors thank the TUBITAK MAG workers for their financial support and acknowledge the contribution of the COST Action CA15107 (MultiComp).

References

[1] C. Liu, F. Li, L.-P. Ma, H.-M. Cheng, Advanced materials for energy storage, Adv. Mater. 22 (2010) E28–E62, https://doi.org/10.1002/adma.200903328.

[2] J. Xu, X. Wang, X. Wang, D. Chen, X. Chen, D. Li, G. Shen, Three-dimensional structural engineering for energy-storage devices: from microscope to macroscope, ChemElectroChem 1 (2014) 975–1002, https://doi.org/10.1002/celc.201400001.

[3] P. Wang, H. Zhou, C. Meng, Z. Wang, K. Akhtar, A. Yuan, Cyanometallic framework-derived hierarchical Co3O4-NiO/graphene foam as high-performance binder-free electrodes for supercapacitors, Chem. Eng. J. 369 (2019) 57–63, https://doi.org/10.1016/j.cej.2019.03.080.

[4] M. Zhu, H. Zhou, J. Shao, J. Feng, A. Yuan, Prussian blue nanocubes supported on graphene foam as superior binder-free anode of lithium-ion batteries, J. Alloy. Comp. 749 (2018) 811–817, https://doi.org/10.1016/j.jallcom.2018.03.378.

[5] J. Zhang, M. Huang, B. Xi, K. Mi, A. Yuan, S. Xiong, Systematic study of effect on enhancing specific capacity and electrochemical behaviors of lithium-sulfur batteries, Adv. Energy Mater. 8 (2018) 1701330, https://doi.org/10.1002/aenm.201701330.

[6] M. Huang, K. Mi, J. Zhang, H. Liu, T. Yu, A. Yuan, Q. Kong, S. Xiong, MOF-derived bi-metal embedded N-doped carbon polyhedral nanocages with enhanced lithium

storage, J. Mater. Chem. A. 5 (2017) 266–274, https://doi.org/10.1039/C6TA09030C.

[7] P.P. Wang, Y.X. Zhang, X.Y. Fan, J.X. Zhong, K. Huang, Synthesis of Si nanosheets by using Sodium Chloride as template for high-performance lithium-ion battery anode material, J. Power Sources 379 (2018) 20–25, https://doi.org/10.1016/j.jpowsour.2018.01.030.

[8] N. Liu, H. Wu, M.T. McDowell, Y. Yao, C. Wang, Y. Cui, A yolk-shell design for stabilized and scalable Li-ion battery alloy anodes, Nano Lett. 12 (2012) 3315–3321, https://doi.org/10.1021/nl3014814.

[9] J. Yang, Y.-X. Wang, S.-L. Chou, R. Zhang, Y. Xu, J. Fan, W. Zhang, H. Kun Liu, D. Zhao, S. Xue Dou, Yolk-shell silicon-mesoporous carbon anode with compact solid electrolyte interphase film for superior lithium-ion batteries, Nano Energy 18 (2015) 133–142, https://doi.org/10.1016/j.nanoen.2015.09.016.

[10] L.Y. Yang, H.Z. Li, J. Liu, Z.Q. Sun, S.S. Tang, M. Lei, Dual yolk-shell structure of carbon and silica-coated silicon for high-performance lithium-ion batteries, Sci. Rep. 5 (2015) 10908, https://doi.org/10.1038/srep10908.

[11] J. Xie, L. Tong, L. Su, Y. Xu, L. Wang, Y. Wang, Core-shell yolk-shell Si@C@Void@C nanohybrids as advanced lithium ion battery anodes with good electronic conductivity and corrosion resistance, J. Power Sources 342 (2017) 529–536, https://doi.org/10.1016/j.jpowsour.2016.12.094.

[12] S. Li, J. Niu, Y.C. Zhao, K.P. So, C. Wang, C.A. Wang, J. Li, Erratum: corrigendum: High-rate aluminium yolk-shell nanoparticle anode for Li-ion battery with long cycle life and ultrahigh capacity, Nat. Commun. 8 (2017) 16174, https://doi.org/10.1038/ncomms16174.

[13] Z. Xing, J. Lu, X. Ji, A brief review of metallothermic reduction reactions for materials preparation, Small Methods 2 (2018) 1800062, https://doi.org/10.1002/smtd.201800062.

[15] Y. Ru, D.G. Evans, H. Zhu, W. Yang, Facile fabrication of yolk–shell structured porous Si–C microspheres as effective anode materials for Li-ion batteries, RSC Adv. 4 (2014) 71–75, https://doi.org/10.1039/C3RA44752A.

[16] S. Zhang, K. Zhao, T. Zhu, J. Li, Electrochemomechanical degradation of high-capacity battery electrode materials, Prog. Mater. Sci. 89 (2017) 479–521, https://doi.org/10.1016/j.pmatsci.2017.04.014.

[17] X. Zuo, J. Zhu, P. Müller-Buschbaum, Y.-J. Cheng, Silicon based lithium-ion battery anodes: a chronicle perspective review, Nano Energy 31 (2017) 113–143, https://doi.org/10.1016/j.nanoen.2016.11.013.

[18] X. Guo, S. Zheng, G. Zhang, X. Xiao, X. Li, Y. Xu, H. Xue, H. Pang, Nanostructured graphene-based materials for flexible energy storage, Energy Storage Mater 9 (2017) 150–169, https://doi.org/10.1016/j.ensm.2017.07.006.

[19] Y. Wimalasiri, L. Zou, Carbon nanotube/graphene composite for enhanced capacitive deionization performance, Carbon N. Y. 59 (2013) 464–471, https://doi.org/10.1016/j.carbon.2013.03.040.

[20] J. Yan, T. Wei, B. Shao, F. Ma, Z. Fan, M. Zhang, C. Zheng, Y. Shang, W. Qian, F. Wei, Electrochemical properties of graphene nanosheet/carbon black composites as electrodes for supercapacitors, Carbon N. Y. 48 (2010) 1731–1737, https://doi.org/10.1016/j.carbon.2010.01.014.

[21] E. Yoo, J. Kim, E. Hosono, H. Zhou, T. Kudo, I. Honma, Large reversible Li storage of graphene nanosheet families for use in rechargeable lithium ion batteries, Nano Lett. 8 (2008) 2277–2282, https://doi.org/10.1021/nl800957b.

[22] M. Alaf, U. Tocoglu, M. Kartal, H. Akbulut, Graphene supported heterogeneous catalysts for Li–O2 batteries, Appl. Surf. Sci. 380 (2016) 185–192, https://doi.org/10.1016/j.apsusc.2016.01.207.

[23] P. Han, A. Manthiram, Boron- and nitrogen-doped reduced graphene oxide coated separators for high-performance Li-S batteries, J. Power Sources 369 (2017) 87–94, https://doi.org/10.1016/j.jpowsour.2017.10.005.

[24] D.C. Marcano, D.V. Kosynkin, J.M. Berlin, A. Sinitskii, Z. Sun, A. Slesarev, L. B. Alemany, W. Lu, J.M. Tour, Improved synthesis of graphene oxide, ACS Nano 4 (2010) 4806–4814, https://doi.org/10.1021/nn1006368.

[25] U. Tocoglu, M. Alaf, O. Cevher, M.O. Guler, H. Akbulut, The effect of oxidants on the formation of multi-walled carbon nanotube buckypaper, J. Nanosci. Nanotechnol. 12 (2012) 9169–9174, https://doi.org/10.1166/jnn.2012.6751.

[26] M. Li, X. Chang, X. Han, W. Yin, M. Ren, Resorcinol-formaldehyde resin based porous carbon materials with yolk-shell structure for high-performance supercapacitors, Synth. Met. 219 (2016) 67–75, https://doi.org/10.1016/j.synthmet.2016.05.011.

[27] X. Fang, S. Liu, J. Zang, C. Xu, M.-S. Zheng, Q.-F. Dong, D. Sun, N. Zheng, Precisely controlled resorcinol–formaldehyde resin coating for fabricating core–shell, hollow, and yolk–shell carbon nanostructures, Nanoscale 5 (2013) 6908, https://doi.org/10.1039/c3nr01723k.

[28] S. Stankovich, D.A. Dikin, R.D. Piner, K.A. Kohlhaas, A. Kleinhammes, Y. Jia, Y. Wu, S.T. Nguyen, R.S. Ruoff, Synthesis of graphene-based nanosheets via chemical reduction of exfoliated graphite oxide, Carbon N. Y. 45 (2007) 1558–1565, https://doi.org/10.1016/j.carbon.2007.02.034.

[29] S. Park, J. An, J.R. Potts, A. Velamakanni, S. Murali, R.S. Ruoff, Hydrazine-reduction of graphite- and graphene oxide, Carbon N. Y. 49 (2011) 3019–3023, https://doi.org/10.1016/j.carbon.2011.02.071.

[30] J. Bai, S.-H. Xing, Y.-Y. Zhu, J.-X. Jiang, J.-H. Zeng, Y. Chen, Polyallylamine-Rh nanosheet nanoassemblies–carbon nanotubes organic-inorganic nanohybrids: a electrocatalyst superior to Pt for the hydrogen evolution reaction, J. Power Sources 385 (2018) 32–38, https://doi.org/10.1016/j.jpowsour.2018.03.022.

[31] X. Zhou, Y. Liu, C. Du, Y. Ren, T. Mu, P. Zuo, G. Yin, Y. Ma, X. Cheng, Y. Gao, Polyaniline-encapsulated silicon on three-dimensional carbon nanotubes foam with enhanced electrochemical performance for lithium-ion batteries, J. Power Sources 381 (2018) 156–163, https://doi.org/10.1016/j.jpowsour.2018.02.009.

[32] B. Li, Y. Jiang, F. Jiang, D. Cao, H. Wang, C. Niu, Bird's nest-like nanographene shell encapsulated Si nanoparticles – their structural and Li anode properties, J. Power Sources 341 (2017) 46–52, https://doi.org/10.1016/j.jpowsour.2016.11.109.

[33] D.M. Chipara, A.C. Chipara, M. Chipara, Raman spectroscopy of carbonaceous materials: a concise review, Spectroscopy 26 (2011) 42–47. http://ezaccess.libraries.psu.edu/login?url=https://search.proquest.com/docview/900723762?accountid=13158%0Ahttp://sk8es4mc2l.search.serialssolutions.com?ctx_ver=Z39.88-2004&ctx_enc=info:ofi/enc:UTF-8&rfr_id=info:sid/ProQ%3Ahightechjournals&rft_val_fmt=in.

[34] S. Chen, W. Yeoh, Q. Liu, G. Wang, Chemical-free synthesis of graphene–carbon nanotube hybrid materials for reversible lithium storage in lithium-ion batteries, Carbon N. Y. 50 (2012) 4557–4565, https://doi.org/10.1016/j.carbon.2012.05.040.

[35] Z. Xing, B. Wang, J.K. Halsted, R. Subashchandrabose, W.F. Stickle, X. Ji, Direct fabrication of nanoporous graphene from graphene oxide by adding a gasification agent to a magnesiothermic reaction, Chem. Commun. 51 (2015) 1969–1971, https://doi.org/10.1039/C4CC08977D.

[36] U. Toçoğlu, G. Hatipoğlu, M. Alaf, F. Kayış, H. Akbulut, Electrochemical characterization of silicon/graphene/MWCNT hybrid lithium-ion battery anodes produced via RF magnetron sputtering, Appl. Surf. Sci. 389 (2016) 507–513, https://doi.org/10.1016/j.apsusc.2016.07.135.

[37] Z. Xing, Y. Qi, Z. Tian, J. Xu, Y. Yuan, C. Bommier, J. Lu, W. Tong, D. Jiang, X. Ji, Identify the removable substructure in carbon activation, Chem. Mater. 29 (2017) 7288–7295, https://doi.org/10.1021/acs.chemmater.7b01937.

[38] Z. Xing, N. Gao, Y. Qi, X. Ji, H. Liu, Influence of enhanced carbon crystallinity of nanoporous graphite on the cathode performance of microbial fuel cells, Carbon N. Y. 115 (2017) 271–278, https://doi.org/10.1016/j.carbon.2017.01.014.

[39] P. Wu, C. Guo, J. Han, K. Yu, X. Dong, G. Yue, H. Yue, Y. Guan, A. Liu, Fabrication of double core–shell Si-based anode materials with nanostructure for lithium-ion battery, RSC Adv. 8 (2018) 9094–9102, https://doi.org/10.1039/C7RA13606D.

[40] Y. Chen, Y. Hu, Z. Shen, R. Chen, X. He, X. Zhang, Y. Li, K. Wu, Hollow core–shell structured silicon@carbon nanoparticles embed in carbon nanofibers as binder-free anodes for lithium-ion batteries, J. Power Sources 342 (2017) 467–475, https://doi.org/10.1016/j.jpowsour.2016.12.089.

[41] Q. Cheng, J. Tang, J. Ma, H. Zhang, N. Shinya, L.-C. Qin, Graphene and carbon nanotube composite electrodes for supercapacitors with ultra-high energy density, Phys. Chem. Chem. Phys. 13 (2011) 17615, https://doi.org/10.1039/c1cp21910c.

[42] W.G. Chong, J.-Q. Huang, Z.-L. Xu, X. Qin, X. Wang, J.-K. Kim, Lithium-sulfur battery cable made from ultralight, flexible graphene/carbon nanotube/sulfur composite fibers, Adv. Funct. Mater. 27 (2017) 1604815, https://doi.org/10.1002/adfm.201604815.

[43] H. Li, C. Lu, B. Zhang, A straightforward approach towards Si@C/graphene nanocomposite and its superior lithium storage performance, Electrochim. Acta 120 (2014) 96–101, https://doi.org/10.1016/j.electacta.2013.12.048.

[44] Y.-S. Ye, X.-L. Xie, J. Rick, F.-C. Chang, B.-J. Hwang, Improved anode materials for lithium-ion batteries comprise non-covalently bonded graphene and silicon nanoparticles, J. Power Sources 247 (2014) 991–998, https://doi.org/10.1016/j.jpowsour.2013.08.048.

[45] Y. Xing, T. Shen, T. Guo, X. Wang, X. Xia, C. Gu, J. Tu, A novel durable double-conductive core-shell structure applying to the synthesis of silicon anode for lithium ion batteries, J. Power Sources 384 (2018) 207–213, https://doi.org/10.1016/j.jpowsour.2018.02.051.

[46] Y. Ma, H. Tang, Y. Zhang, Z. Li, X. Zhang, Z. Tang, Facile synthesis of Si-C nanocomposites with yolk-shell structure as an anode for lithium-ion batteries, J. Alloy. Comp. 704 (2017) 599–606, https://doi.org/10.1016/j.jallcom.2017.02.083.

[47] D. Yao, Y. Yang, Y. Deng, C. Wang, Flexible polyimides through one-pot synthesis as water-soluble binders for silicon anodes in lithium ion batteries, J. Power Sources 379 (2018) 26–32, https://doi.org/10.1016/j.jpowsour.2017.12.086.